A combination of seismic refraction and ambient noise methods to detect landslide-prone materials

Martín Cárdenas-Soto[1] ⓘ, Jesús Sánchez-González[1] ⓘ, José Antonio Martínez-González[1] ⓘ, David Escobedo-Zenil[1] ⓘ, Gerardo Cifuentes-Nava[2] ⓘ, Thalía Alfonsina Reyes-Pimentel[1] ⓘ

Abstract

A portion of the west of Mexico City is densely populated in an abrupt topography, whose volcano-sedimentary materials increase the likelihood of landslides. We exploited the geometry of a quadrangular geophones array to apply Seismic Refraction Tomography (SRT) and Ambient Noise Tomography (ANT) methods and explore the extent of landslide-prone materials. The results show low-velocity areas (Vs < 100 m/s, being Vs group velocities) associated with materials that have lost their resistance due to the increase in pore pressure and the places where eventually, more landslides will occur (120 < Vs < 200 m/s) if mitigation work is not carried out. The most stable zones correspond to materials with velocity values greater than 250 m/s that overlap a bedrock at an average depth of 8 m. Thus, when it is not advisable to perform active source experiments, ANT can provide practical results to determine the extension of the sliding materials.

Resumen

Una porción del poniente de la Ciudad de México está densamente poblada en una topografía abrupta. Los materiales en esa zona son volcano-sedimentarios, los cuales, debido a procesos naturales y antropogénicos, aumentan la probabilidad de deslizamientos de tierra. En este estudio explotamos la geometría de un arreglo cuadrangular de geófonos mediante los métodos de Tomografía de Refracción Sísmica (TRS) y Tomografía de Ruido Ambiental (TRA) para explorar la extensión de los materiales propensos a deslizamientos de tierra. Los resultados muestran áreas de baja velocidad (Vs < 100 m/s) asociadas con materiales que han perdido su resistencia debido al aumento de la presión de poro, y áreas donde eventualmente ocurrirán más deslizamientos de tierra (120 < Vs < 200 m/s) si no se realizan trabajos de mitigación. Las zonas más estables corresponden a materiales con valores de velocidad superiores a 250 m/s que sobreyacen a un subestrato irregular con profundidad media de 8 m. Por lo tanto, cuando no es aconsejable realizar experimentos de fuente activa, TRA puede proporcionar resultados prácticos para determinar la extensión de los materiales propensos a deslizamiento.

1. Introduction

The effects of complex geology, terrain subsidence, or cavities occur in the first-meter depth. Therefore, characterizing the subsoil in those first meters by near-surface geophysics techniques is essential to implementing mitigation and damage prevention measures in the service of society (Everett, 2013). However, each method is required to obtain a reasonable vertical and horizontal resolution of the subsoil's physical properties, so applying at least to geophysical methods is always recommended (Gabàs *et al.*, 2013). For example, water extraction (or some other related phenomenon) complicates the subsoil homogeneity, producing subsidence and fracturing of the terrain, including cavities, and the human infrastructure is almost always damaged. In such conditions, the subsoil characterization with different irregularities requires analyzing and confronting the results of different geophysical methods since the distribution of the material soil properties occurs at different scales (Romero-Ruiz *et al.*, 2018).

Landslides are highly prevalent natural disasters that inflict significant losses across multiple domains of human existence. The landslide term encompasses several forms of mass movement down a slope, comprising soil, rock, debris, organic materials, artificial fill, or a combination thereof (Varnes, 1958). The stability of slopes is typically associated with the gravitational equilibrium between the elements that induce shear stress and the characteristics that provide resistance to soil mass movement (Alimohammadlou *et al.*, 2013). In addition, sudden landslides occur under a stress regime in which the land mass is affected by extraordinary precipitation, or the induced stress caused by an earthquake (Jongmans and Garambois, 2007). Electrical resistivity tomography and active seismic methods are the most systematic geophysical methods for studying landslides (Perrone *et al.*, 2014). These methods offer broader spatial coverage than geotechnical investigations to quantify the variability and physical state of the hydrogeological parameters associated with the sliding surface (Uhlemann *et al.*, 2016). Traditional seismic methods for subsurface characterization include seismic refraction and spectral analysis of surface waves (whether from an active or passive source) to obtain, more accurately, the bedrock irregularity (Harba *et al.*, 2019; Uhlemann *et al.*, 2016; Zainal *et al.*, 2021). However, to cover large areas or acquire data in topographically complicated terrain, the results could be only a sample of the magnitude of the problem in the case of landslides.

Ambient Noise Tomography (ANT) has become popular in the last decade to characterize the subsoil structure. The principle of the method is based on Seismic Interferometry, the cross-correlation of recorded seismic noise to extract the so-called Empirical Green Function (EGF, Campillo and Paul, 2003; Shapiro and Campillo, 2004). Given the broad spectrum of seismic noise, and since the noise is mainly composed of surface waves (Nakata *et al.*, 2019), it has been used at different scales to characterize the subsurface structure, producing a 3D image of subsurface velocity (Ritzwoller, 2009). The success in recovering the EGF depends mainly on the nature and distribution of noise sources between receivers. A summary of the historical background and various applications in science and engineering tasks are described by Larose *et al.* (2015) and Schuster (2014). For example, in the case of landslides, Seismic Interferometry has been used to identify the extent of the elastic properties contrast between the soft materials and the bedrock (Renalier *et al.*, 2010; Pilz *et al.*, 2013; Harba *et al.*, 2019; Chávez-García *et al.*, 2021). Additionally, the coda of the EGFs has allowed monitoring to detect velocity changes before the potential mass motions (Mainsant *et al.*, 2012; Del Gaudio *et al.*, 2013; Breton *et al.*, 2021).

Mexico City is a densely populated city. Its western side is topographically abrupt, and the geological risk is increased because the subsoil structure is composed of volcano-sedimentary materials, which were exploited economically in the mid-twentieth century, leaving a series of underground mines. In addition, the geological risk is increased because the subsoil structure is interspersed with silt-sandy materials, clasts, and tuffs, originated by pyroclastic-detritus flows and ash deposits susceptible to landslides (Arce *et al.*, 2019). A small ecological-sustainable park is at risk of disappearing in that area due to landslides caused by underground runoff and leaks in drainage systems. The Park is located on the bank of a reforested piedmont (19.344433 N, 99.232400 W), bordered by a river. It is a residential area where vegetable planting is carried out, and the inhabitants use it as a recreational area (Figure 1). This work aims to determine the lateral extent of materials prone to landslides by analyzing velocity images obtained from Seismic Refraction Tomography (SRT), surface waves produced by the seismic refraction method, and ANT.

2. Method

We use two arrays to explore the velocity contrasts in the study area, a linear and semi-enclosed array, each of 24-4.5 Hz vertical component geophones separated every 5 m to conduct active source (using a sledgehammer in front of each geophone) and ambient noise seismic acquisitions (Figure 1a). The records produced by seismic sources were processed to obtain three different results. First, we produced a 2D Vp velocity model along the linear array (SE-NE direction, see Figure 1) using SRT (Stefani, 1995; Guedes, 2022). The low-velocity zones in this model were confronted with Electric Resistivity Tomography (ERT). Subsequently, the area inside the semi-enclosed array was discretized with cells proportional to receiver separation. Then,
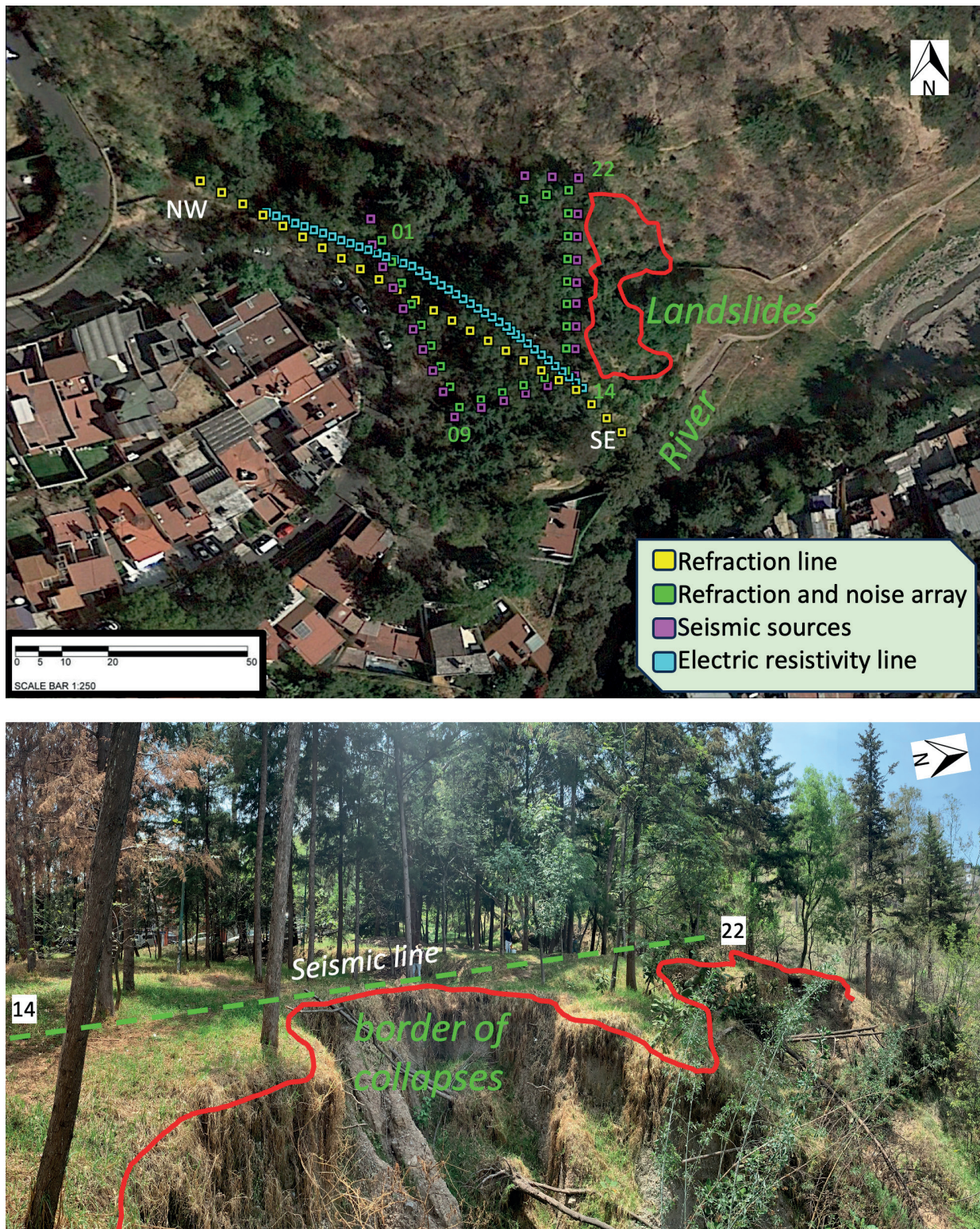
Figure 1. Upper image: site study area and array geometry of the geophysics studies. The geophone number is indicated at the vertices on the semi-closed seismic array. Lower image: lateral view of the landslides. The dashed green line indicates the refraction profile between geophones 14 and 22. The red line denotes the limits of the landslides.

the refracted time arrivals at each cell were linearly adjusted to obtain the slope inverse (Vp) and the intercept time to estimate the bedrock depth (Cárdenas-Soto *et al.*, 2022) using the Vp near surface average obtained on the linear array. In a second step, we obtained group velocity dispersion curves from the surface waves (Herrmann, 2013) of the refraction records and those extracted from seismic noise cross-correlations. Those curves let us calculate time groups, which were inverted to construct velocity group images (here referred Vs tomography images) in the 4.5 – 32 Hz frequency range.

3. Seismic refraction and ERT results

Figure 2a shows an example of seismic refraction records. First arrivals are well-identified on the useful seismic traces. The spectral amplitude indicates that source energy was concentrated near 50 Hz, and the surface waves were well developed for frequencies at least larger than 15 Hz. The first arrivals were processed using the pyGIMLi software, which uses Pearson's chi-squared test to assess the presence of a statistically significant disparity between the anticipated and observed data. The data fitting criteria for SRT were met after four iterations, as indicated by a Chi2 value of less than or equal to 1. A more detailed explanation of the seismic tomography method is provided in the next section. The SRT of the linear array, apparently located on the most stable side of the park, is shown in Figure 2b. A soft

layer is observed at the lower slope with Vp values less than 400 m/s, typical velocities of weathered materials (Telford *et al.*, 1990). The line extension allows the definition of a second layer with an irregular structure with poorly consolidated materials (Vp=800 m/s). Vp values greater than 1200 m/s can be associated with the bedrock at depths greater than 10 m; particularly, a high-velocity anomaly at the center of the line stands out. These results show that the low-velocity values correspond to backfill deposits (probably partially saturated) susceptible to slipping due to underground water flow caused by a damaged drainage system (observed in the site) in the highest part of the refraction line.

To corroborate the presence of saturated materials, we obtained an image of ERT in the same direction as the seismic line (Figure 1). To do this, an Iris Instruments brand resistivimeter, Syscal Pro Switch model, was used, which recorded data on a Wenner-Schlumberger array of 48 electrodes with a sampling between 3-6 cycles per second. We used the EarthImager2D software (AGI, 2014) to make a robust inversion of 8 iterations until the RMS error was reduced to less than 10%, a common practice in electrical prospecting studies using commercial software (Loke, 2004). Figure 2c shows the ERT section, where it is observed that the maximum depth of investigation is approximately 15 m, and the resistivity distribution has values less than 50 ohm-m corresponding to partially saturated materials. The penetration depth does not allow the water table identification, which probably corresponds to the high-velocity interface identified in the refraction section (Figure 2b).
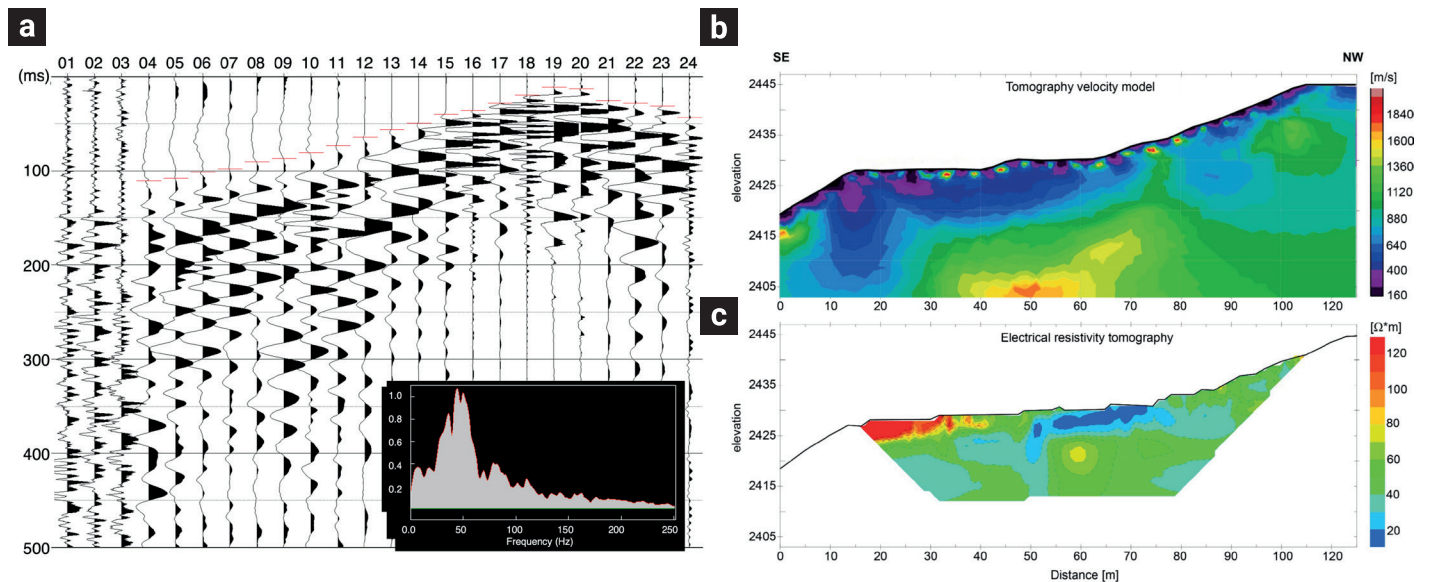

Figure 2. a) Seismic traces and amplitude spectrum (red marks indicate first picks). b) Seismic refraction tomography and c) Electric resistivity tomography oriented in the SE-NW direction (see Figure 1).

4. Active and Passive 3D Seismic Tomography

In traveltime tomography, the inverse problem is solved with traveltimes and ray paths, and raytracing needs to be done again iteratively (Girous and Larouche, 2013). The Shortest Path approach (Moser, 1991) with secondary nodes (Giroux and Larouche, 2013) is the fundamental algorithm of pyGIMLi software. The tomography pictures of seismic refraction or time groups were generated using the pygimli.physics.traveltime module of the pyGIMLi, as described by Rücker *et al.* (2017). The inversion approach relies on several meshes. The mesh used in this study is characterized by a coarse resolution representing the cells in which the velocities are determined and where the algorithm finds the shortest path from source to receiver, solving a linear system of equations.

The inversion approach adopted in this study utilizes the Gauss-Newton method with an inexact line search (Martínez and Qi, 1995), following the methodology proposed by Günther *et al.* (2006). The process of reducing the discrepancy between the observed data and the predicted response of a model is achieved by utilizing the L2-Norm, resulting in the least-squares approach. An error-weighting technique is employed to address the presence of data mistakes, which leads to the optimization of the data objective function. The process of inversion often starts by utilizing an initial model, which commonly consists of a subsurface that is horizontally stratified and has progressively increasing velocities. Successive iterations are performed until the objective function, or the absolute RMS misfit is less than 0.5%. The extent of data coverage determines the visibility of the inversion findings. This metric reflects the degree to which model cells contribute to the dataset.

Figure 3a displays the absolute root mean square (RMS) misfit of the group time inversions of both active and passive seismic data throughout the examined frequency range. A contrasting pattern is evident for frequencies below 15 Hz; the inversion of seismic noise data exhibits superior fitting due to its higher content of low-frequency surface waves (Nakata *et al.*, 2019). In contrast, active seismic methods generate surface waves with energy at higher frequencies. Adjusting passive data has a favorable conformity when the frequency surpasses 15 Hz. The observed trend can be attributed to the reduced variability in seismic velocities within the higher layer. This phenomenon is also evident in the group time inversion of surface waves produced by the refraction method, where the RMS remains relatively constant up to frequencies of 32 Hz. The procedure of inverting group timings for individual frequencies involved a comprehensive investigation of cell coverage. Figures 3a and 3c depict the cell coverage at a frequency of 16 Hz for both datasets. Most cells exhibited a trajectory count exceeding 50,

with some surpassing 100. Similar results are observed for the other frequencies.

4.1. Seismic refraction tomographies

The semi-enclosed array lets us explore more significant area extension by building a pseudo-3D Vp in-depth image of refracted arrivals and another of Vs using dispersion curves, both active source tomographies. Figure 4a shows the first arrival selection of all refraction shot records. Direct arrivals show that Vp in the first layer is approximately 400 m/s. Refracted arrivals (after a critical distance of 20 m) exhibit large dispersion, indicating the bedrock is irregular with a Vp average of 1200 m/s according to the values in Figure 4a. Figure 4b shows the velocities representation of the discretized model (the best fit of first-time arrivals to seismic refraction equation, e.g., a line). A higher velocity zone is observed in the northern part of the array, between 8 and 10 m depth, with Vp reaching up to 3000 m/s. In general, the bedrock average depth is 8 m, according to the results of Figure 2b. The best-fit error was quantified by the RMS of the residuals shown in Figure 4c, where we observe the highest errors near the high Vp zone.

The group velocity dispersion curves extracted from each seismic refraction record (a source-receiver distance greater than 15 m) are shown in Figure 5a. A strong tendency of these curves indicates that acceptable values are greater than 8 Hz (below this frequency, there is no energy). That trend shows the slight dependence of velocity as a function of frequency, but it is practically constant. We obtained different tomographies between the frequencies from 5 to 30 Hz. However, their differences are insignificant, given the constant tendency of dispersion curves. Figure 5b exhibits a representative tomography at 20 Hz. In that figure, we can observe a high-velocity zone at the central array bordered by low-velocity zones correlated (by the direct observations on the site) to saturation on the western side and materials susceptible to sliding on the eastern side.

4.2. Ambient Noise Tomography

Similarly to the active surface wave dispersion study, ANT images were obtained in the same frequency range using the dispersion curves extracted from noise cross-correlation. One standard method of preprocessing noise data involves performing one-bit normalization to remove transient events and using spectral whitening to equalize the spectra (Bensen *et al.*, 2007). This work shows that using spectral whitening alone is sufficient for capturing reasonably accurate dispersion curves. Subsequently, cross-correlations are performed among all receiver pairs between 8-second intervals over 30 minutes to derive the

EGFs, also known as Empirical Green's Functions. Figure 6a shows an example of a virtual source gather (Bakulin & Calvert, 2006) for the geophone 11 filtered between 8 and 24 Hz. The observed well-developed pulses represent surface waves with an acausal essence due to a non-uniform noise source distribution (Tsai, 2011). In addition, late waveforms (delay times larger than 4 s), produced by the low-velocity zones, are observed in some correlograms. Subsequently, we stack acausal and causal parts of these functions and get group velocity dispersion curves.

Figure 6b shows the dispersion curves obtained from the noise cross-correlations between the pairs of receivers with interdistances larger than 15 m. A uniform trend of these curves is observed at frequencies greater than 7 Hz. In the same way,

as in the case of the active source, Figure 6c shows the results at 20 Hz. We can observe large velocity values (400 m/s) at the array center concerning the borders (less than 200 m/s). The velocity distribution is comparable to that obtained by active source records (Figure 5b) but with slightly lower values. Values close to 100 m/s indicate the areas of softer or highly saturated materials (as indicated by the ERT section). Such materials are prone to slip between geophones 24 and 42 (according to direct observations in the eastern part of the array). Velocities more significant than 300 m/s, corresponding to compact materials, are observed at the array center and correlate with the high-velocity zone resolved by refraction tomography (Figures 2b and 4b). Differences in the velocity distribution are due to the nature
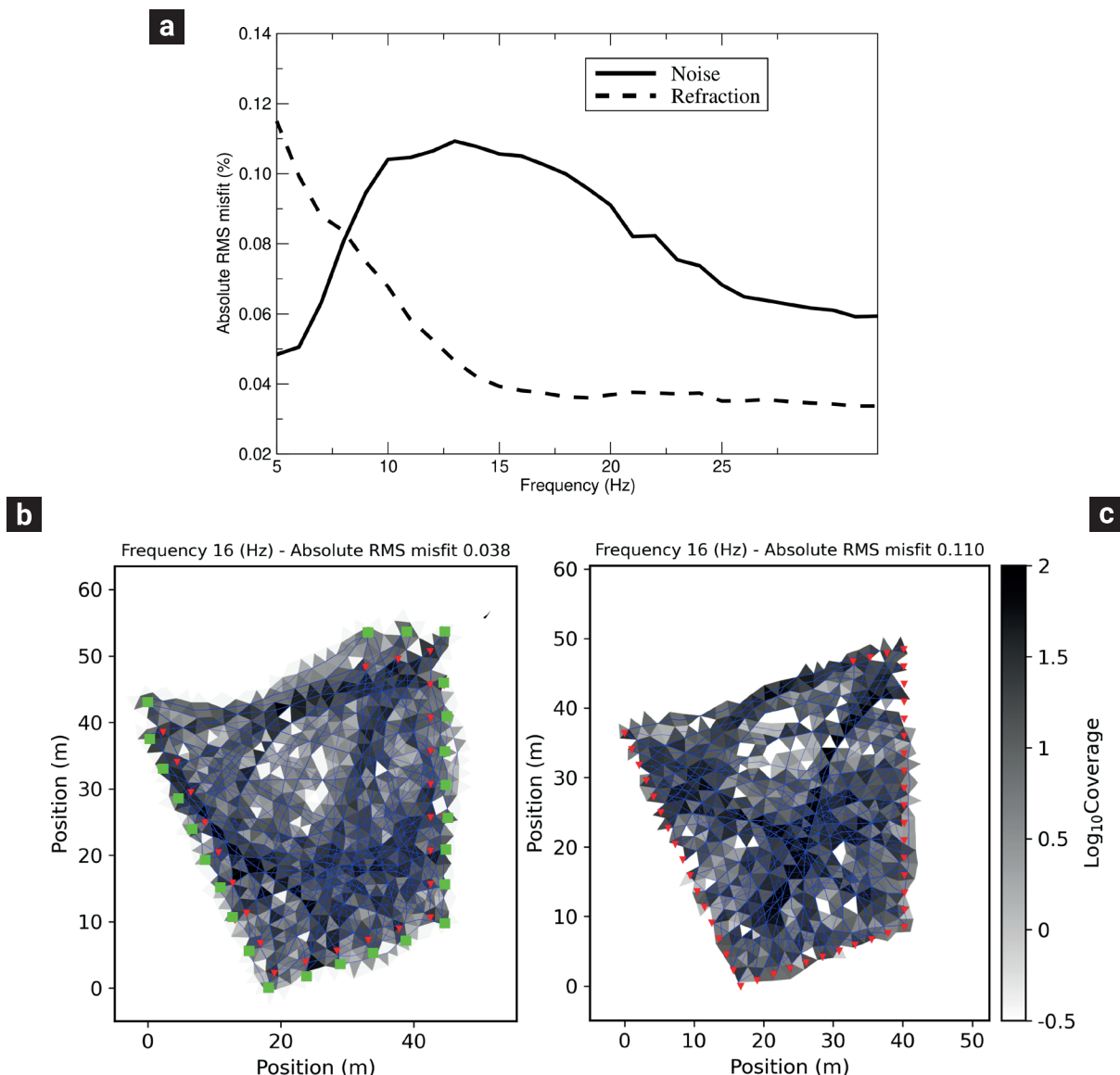

Figure 3. a) Absolute RMS misfit after the final interaction of times group inversion at each frequency. b) and c) Cell coverage for the active and passive data, respectively. Red triangles indicate the geophone position and green squares are the source position for the active experiment.
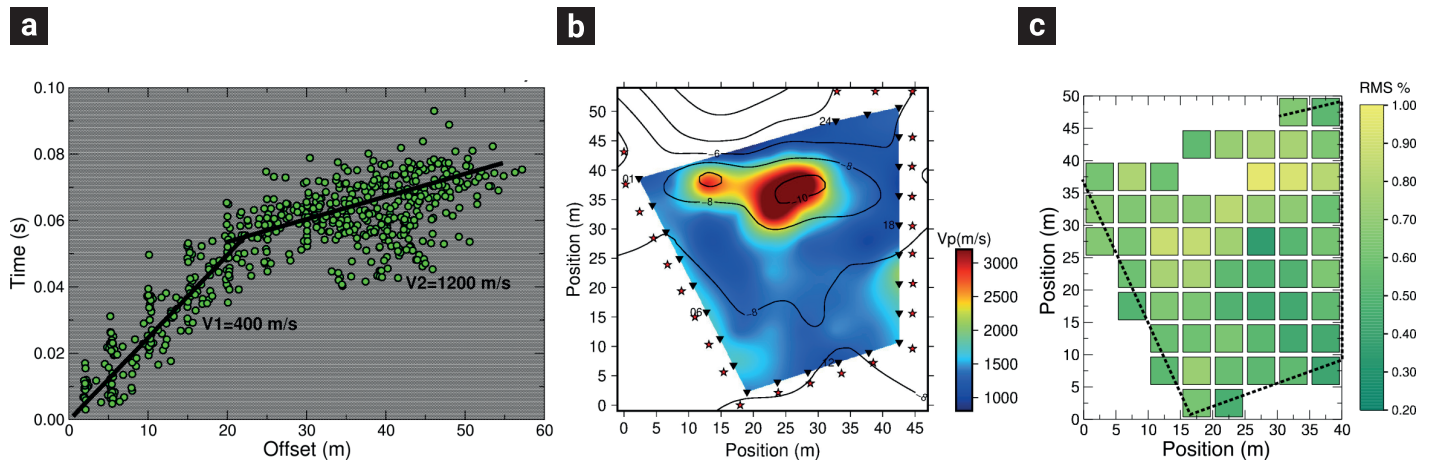
Figure 4. a) First arrival travel times (green circles) at all receivers due to all sources. Vp velocities of the first and second layers are indicated. b) Vp tomography obtained from sources and receptors at the surface. Open black circles indicate the geophone's position. c) Error percentage of the best-fit line of refracted arrivals.
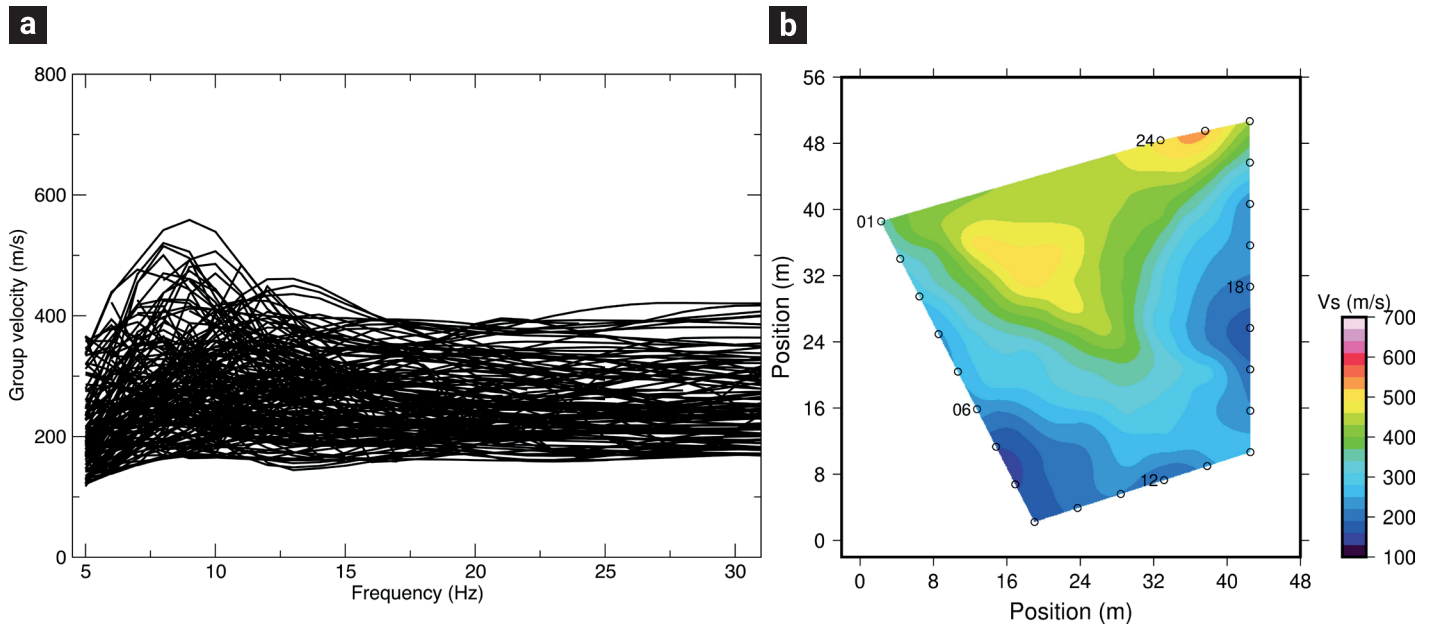

Figure 5. a) Dispersion curves obtained from active source records for source-receiver distances larger than 15 m. b) Group velocity tomography image at 20 Hz. Open black circles indicate the position of the geophones.

of surface waves and the lack of coverage in the northern part of the array. Furthermore, ambient noise tomographies for frequencies below 24 Hz (not shown here for brevity) corroborate the existence of such anomaly at greater depth.

The construction of a 3D model of Vs using ANT allows us to outline the extent of the materials prone to falling (Renalier *et al.*, 2010; Pilz *et al.*, 2014). The procedure generally involves extracting and selecting dispersion curves from the tomography results and subsequently inverting these to derive the best velocity model. In this work, we have followed a simple procedure

by stacking the Vs tomography images in the frequency range of 10 to 24 Hz. Then, the frequency was converted to vertical wavelength (or pseudo depth) following Cárdenas-Soto *et al.*, (2016; 2021a, b). Figure 7 shows this model, which emphasizes the zone defined by velocities larger than 350 m/s concerning those less than 200 m/s. The figure also allows us to appreciate the bedrock irregularity (according to the refraction results) and the extension of materials susceptible to sliding, two essential parameters to understanding landslide behavior and taking the necessary mitigation measures.
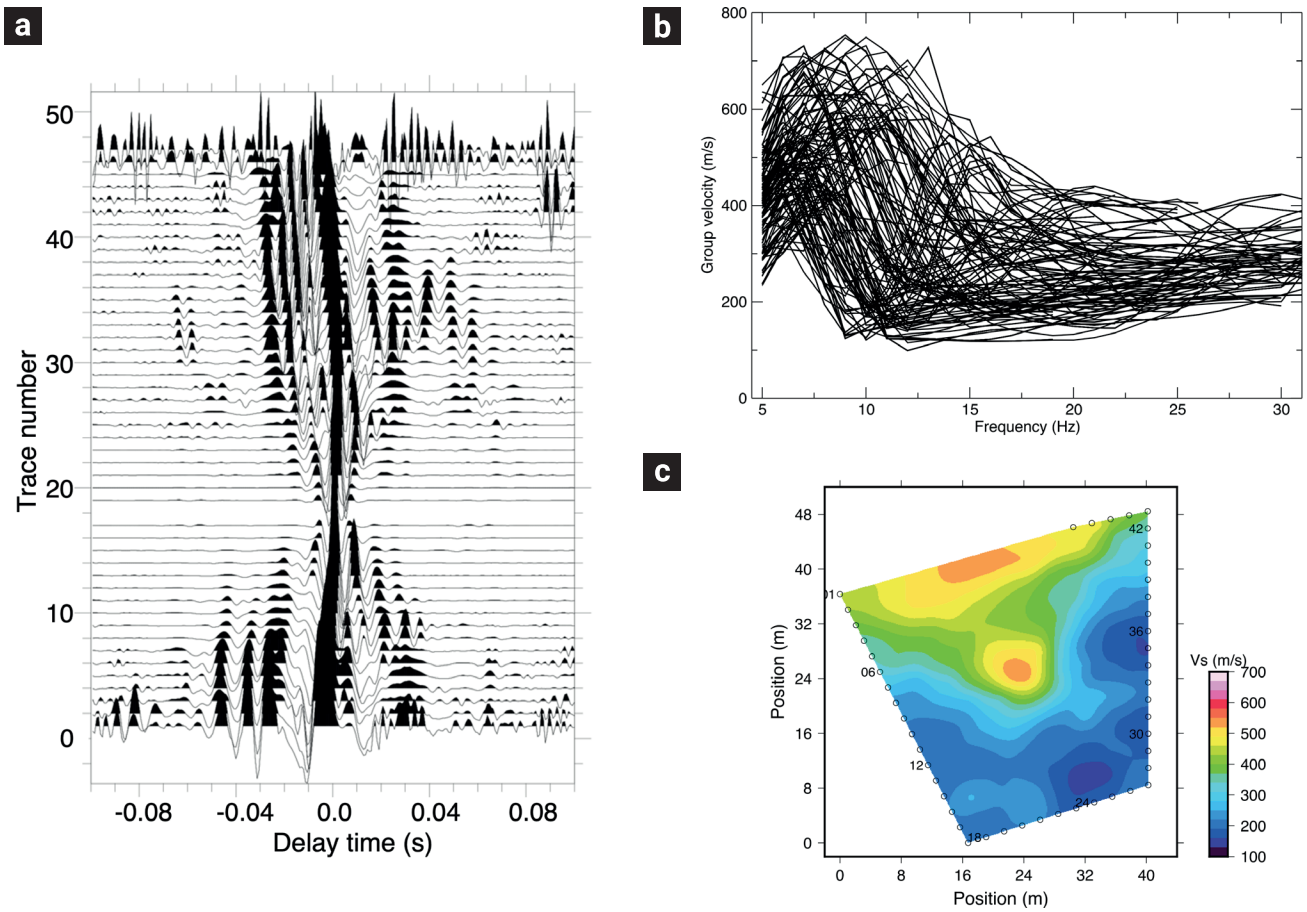
Figure 6. a) Virtual source gather for the geophone number 11. Cross-correlation waveforms are bandpass filtered between 8 and 24 Hz. b) Dispersion curves obtained from noise cross-correlation for interdistances larger than 15 m. c) Group velocity tomography at 20 Hz. Open black circles indicate the position of the geophones.
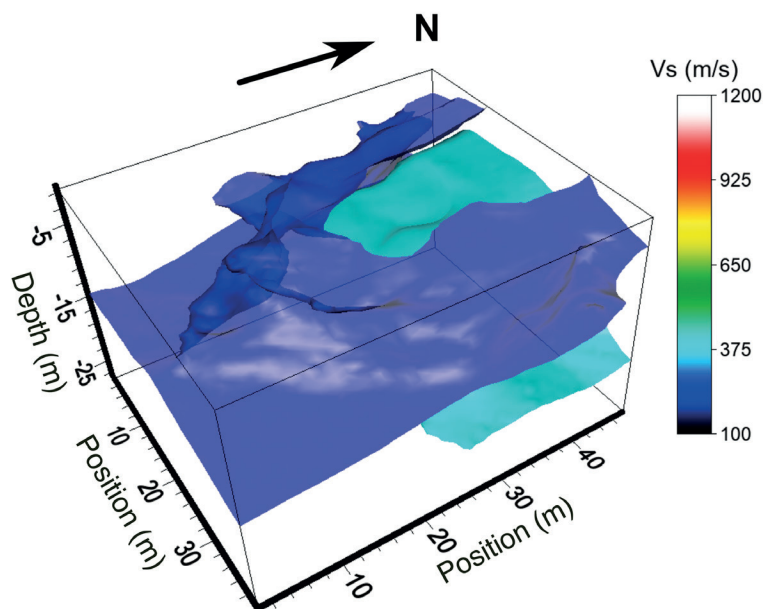

Figure 7. 3D velocity model built from the stack of 2D tomographies. The model highlights the velocity isosurfaces of 150 and 400 m/s.

5. Conclusions

A quadrangular seismic array has allowed us to explore the structure of the subsurface using seismic refraction methods and ambient seismic noise interferometry. The combination of active and passive source methodologies (in this case, seismic noise) allowed us to obtain images of the compressional velocity distribution (Vp) and surface wave velocity group (here called Vs) of materials prone to landslides. The refraction method reasonably determined the bedrock depth, which can also be inferred by the arrival times of the semi-closed array of sources and receivers on the surface. The surface waves generated from the active source and extracted from the ambient noise allowed us to delineate the extent of materials close to the slide, whose Vs values below 200 m/s contrast markedly with the area of more compact materials. We found that the best Vs rate correlation obtained from both methods is at an average frequency of 20 Hz. However, the results leading to a higher resolution of the subsurface structure can be obtained by ANT at a higher. Therefore, in the case of increased landslide risk, when it is not advisable to induce stresses in the subsoil, ambient seismic noise can provide practical results for determining the extent of sliding materials.

6. Acknowledgments

7. Data Accessibility

The data supporting the findings of this study are available from the corresponding author upon reasonable request.

8. References

Advanced Geosciences, Inc. (2014). Instruction manual for EarthImager 2D, version 1.9.0, Resistivity and IP inversion software: Advanced Geosciences, Inc.,134 p., accessed at **http://www.agiusa.com/**

Alimohammadlou, Y., Najafi, A., & Yalcin, A. (2013). Landslide process and impacts: A proposed classification method. *Catena*, 104, 219-232. doi: **https://doi.org/10.1016/j.catena.2012.11.013**

Arce, J. L., Paul, W. L., Luis Macías, J., Morales-Casique, E., García-Palomo, A., Jiménez-Domínguez, F. J., Benowitz, J., & Vásquez-Serrano, A. (2019). Geology and Stratigraphy of the Mexico Basin (Mexico City) Central Trans-Mexican Volcanic Belt. *Journal of Maps* 15(2), 320–32. doi: **https://doi.org/10.1080/17445647.2019.1593251**

Bakulin, A., & Calvert, R. (2006). The virtual source method: Theory and case study. *Geophysics*, 71(4), SI139-SI150. doi: **https://doi.org/10.1190/1.2216190**

Bensen, G. D., Ritzwoller, M. H., Barmin, M. P., Levshin, A. L., Lin, F., Moschetti, M. P., Shapiro, N. M., & Yang, Y. (2007). Processing Seismic Ambient Noise Data to Obtain Reliable Broad-Band Surface Wave Dispersion Measurements. *Geophysical Journal International* 169(3), 1239–60. doi: **https://doi.org/10.1111/j.1365-246x.2007.03374.x**

Breton, M. L., Bontemps, N., Guillemot, A., Baillet, L., & Larose, E. (2021). Landslide Monitoring Using Seismic Ambient Noise Correlation: Challenges and Applications. *Earth-Science Reviews* 216 (May): 103518. doi: **https://doi.org/10.1016/j.earscirev.2021.103518**

Campillo, M., & Paul, A. (2003). Long-Range Correlations in the Diffuse Seismic Coda. Science 299 (5606), 547–49. doi: **https://doi.org/10.1126/science.1078551**

Cárdenas-Soto, M., Ramos-Saldaña, H., & Vidal-García, M. C. (2016). Interferometría de ruido sísmico para la caracterización de la estructura de velocidad 3D de un talud en la 3ª Sección del Bosque de Chapultepec, Ciudad de México. *Boletín de la Sociedad Geológica Mexicana*, 68(2), 173-186. doi: **https://doi.org/10.18268/bsgm2016v68n2a1**

Cárdenas-Soto, M., Piña-Flores, J., Escobedo-Zenil, D., Sánchez-González, J., & Martínez-González, J. A. (2021a). Ambient seismic noise tomography to build up a 3D shear-wave velocity model. *Ingeniería, investigación y tecnología*, 22(2), 1-9. doi: **https://doi.org/10.22201/fi.25940732e.2021.22.2.009**

Cárdenas-Soto, M., Piña-Flores, J., Escobedo-Zenil, D., Vidal-Garcia, M. C., Natarajan, T., Hussain, Y., and Sánchez-Sesma F. J. (2021b). Seismic Ambient Noise Tomography to Retrieve near-Surface Properties in Soils with Significant 3D Lateral Heterogeneity: The Case of Quinta Colorada Building in Chapultepec Mexico. *Natural Hazards* 108(1), 129–45. doi: **https://doi.org/10.1007/s11069-021-04735-4**

Cárdenas-Soto, M., Gámez Lindoro, J. A., Peña Gaspar, V., Aguirre Díaz, J. P., & García Serrano, A. (2022). A Pseudo 3D Seismic Refraction Tomography for Exploring Archaeological Structures. *Ingeniería Investigación y Tecnología* 23(1), 1–9. doi: **https://doi.org/10.22201/fi.25940732e.2022.23.1.003**

Chávez-García, F. J., Natarajan, T., Cárdenas-Soto, M., & Rajendran, K. (2021). Landslide characterization using active and passive seismic imaging techniques: a case study from Kerala, India. *Natural Hazards*, 105, 1623-1642. doi: **https://doi.org/10.1007/s11069-020-04369-y**

Del Gaudio, V., Wasowski, J., & Muscillo, S. (2013). New developments in ambient noise analysis to characterise the seismic response of landslide-prone slopes. *Natural hazards and earth system sciences*, 13(8), 2075-2087. doi: **https://doi.org/10.5194/nhess-13-2075-2013**

Everett, Mark E. (2013). Near-Surface Applied Geophysics. *Cambridge University Press*. doi: **https://doi.org/10.1017/CBO9781139088435**

Gabàs, A., Macau, A., Benjumea, B., Bellmunt, F., Figueras, S., & Vilà, M. (2014). Combination of geophysical methods to support urban geological mapping. *Surveys in Geophysics*, 35, 983-1002. doi: **https://**

doi.org/10.1007/s10712-013-9248-9

Giroux, B., & Larouche, B. (2013). Task-parallel implementation of 3D shortest path raytracing for geophysical applications. *Computers & geosciences*, 54, 130-141. doi: https://doi.org/10.1016/j.cageo.2012.12.005

Guedes, V. J. C. B., Maciel, S. T. R., & Rocha, M. P. (2022). Refrapy: A Python program for seismic refraction data analysis. *Computers & Geosciences*, 159, 105020. doi: https://doi.org/10.1016/j.cageo.2021.105020

Günther, T., Rücker, C., & Spitzer, K. (2006). Three-dimensional modelling and inversion of DC resistivity data incorporating topography—II. Inversion. *Geophysical Journal International*, 166(2), 506-517. doi: https://doi.org/10.1111/j.1365-246X.2006.03011.x

Harba, P., Pilecki, Z., & Krawiec, K. (2019). Comparison of MASW and seismic interferometry with use of ambient noise for estimation of S-wave velocity field in landslide subsurface. *Acta Geophysica*, 67(6), 1875-1883. doi: https://doi.org/10.1007/s11600-019-00344-9

Herrmann, R. B. (2013). Computer programs in seismology: An evolving tool for instruction and research. *Seismological Research Letters*, 84(6), 1081-1088. doi: https://doi.org/10.1785/0220110096

Jongmans, D., & Garambois, S. (2007). Geophysical investigation of landslides: a review. *Bulletin de la Société Géologique de France*, 178(2), 101-112. doi: https://doi.org/10.2113/gssgfbull.178.2.101

Larose, E., Carrière, S., Voisin, C., Bottelin, P., Baillet, L., Guéguen, P., & Massey, C. (2015). Environmental seismology: What can we learn on earth surface processes with ambient noise? *Journal of Applied Geophysics*, 116, 62-74. doi: https://doi.org/10.1016/j.jappgeo.2015.02.001

Loke, M. H. (2004). Tutorial: 2-D and 3-D electrical imaging surveys.

Mainsant, G., Larose, E., Brönnimann, C., Jongmans, D., Michoud, C., & Jaboyedoff, M. (2012). Ambient seismic noise monitoring of a clay landslide: Toward failure prediction. *Journal of Geophysical Research: Earth Surface*, 117(F1). doi: https://doi.org/10.1029/2011jf002159

Martínez, J., & Qi, L. (1995). Inexact Newton methods for solving nonsmooth equations. *Journal of Computational and Applied Mathematics*, 60(1-2), 127-145. doi: https://doi.org/10.1016/0377-0427(94)00088-I

Moser, T. J. (1991). Shortest path calculation of seismic rays. *Geophysics*, 56(1), 59-67. doi: https://doi.org/10.1190/1.1442958

Nakata, N., Gualtieri, L., & Fichtner, A. (Eds.). (2019). Seismic ambient noise. *Cambridge University Press*. doi: https://doi.org/10.1017/9781108264808

Perrone, A., Lapenna, V., & Piscitelli, S. (2014). Electrical resistivity tomography technique for landslide investigation: A review. *Earth-Science Reviews*, 135, 65-82. doi: https://doi.org/10.1016/j.earscirev.2014.04.002

Pilz, M., Parolai, S., Bindi, D., Saponaro, A., & Abdybachaev, U. (2014). Combining seismic noise techniques for landslide characterization. *Pure and Applied Geophysics*, 171, 1729-1745. doi: https://doi.org/10.1007/s00024-013-0733-3

Renalier, F., Jongmans, D., Campillo, M., & Bard, P. Y. (2010). Shear wave velocity imaging of the Avignonet landslide (France) using ambient noise cross correlation. *Journal of Geophysical Research: Earth Surface*, 115(F3). doi: https://doi.org/10.1029/2009jf001538

Ritzwoller, M. H. (2009). Ambient noise seismic imaging. *Recent Development in World Seismology*, 9(31), 315-328. doi: https://doi.org/10.1036/1097-8542.YB090130

Romero-Ruiz, A., Linde, N., Keller, T., & Or, D. (2018). A review of geophysical methods for soil structure characterization. *Reviews of Geophysics*, 56(4), 672-697. doi: https://doi.org/10.1029/2018rg000611

Rücker, C., Günther, T., & Wagner, F. M. (2017). pyGIMLi: An open-source library for modelling and inversion in geophysics. *Computers & Geosciences*, 109, 106-123. doi: https://doi.org/10.1016/j.cageo.2017.07.011

Schuster, G. T. (2014). Seismic interferometry. In Encyclopedia of exploration geophysics (pp. Q1-1). *Society of Exploration Geophysicists*. doi: https://doi.org/10.1190/1.9781560803027

Shapiro, N. M., & Campillo, M. (2004). Emergence of broadband Rayleigh waves from correlations of the ambient seismic noise. *Geophysical Research Letters*, 31(7). doi: https://doi.org/10.1029/2004gl019491

Stefani, J. P. (1995). Turning-ray tomography. *Geophysics*, 60(6), 1917-1929. doi: https://doi.org/10.1190/1.1443923

Telford, W. M., Geldart, L. P., & Sheriff, R. E. (1990). Applied Geophysics Cambridge *University Press Cambridge*. United Kingdom. doi: https://doi.org/10.1017/cbo9781139167932

Tsai, V. C. (2011). Understanding the amplitudes of noise correlation measurements. *Journal of Geophysical Research: Solid Earth*, 116(B9). doi: https://doi.org/10.1029/2011jb008483

Uhlemann, S., Hagedorn, S., Dashwood, B., Maurer, H., Gunn, D., Dijkstra, T., & Chambers, J. (2016). Landslide characterization using P-and S-wave seismic refraction tomography—The importance of elastic moduli. *Journal of Applied Geophysics*, 134, 64-76. doi: https://doi.org/10.1016/j.jappgeo.2016.08.014

Varnes, D. J. (1958). Landslide types and processes: Landslides and Engineering Practice by the Committee on Landslide Investigations: in Eckel. Highway Research Board Special Report, 29.

Zainal, M., Munir, B., Marwan, M., Yanis, M., & Muhni, A. (2021). Characterization of Landslide geometry using Seismic Refraction Tomography in the GayoLues, Indonesia. *Journal of Physics and Its Applications*, 3(2), 148-154. doi: https://doi.org/10.14710/jpa.v3i2.10601